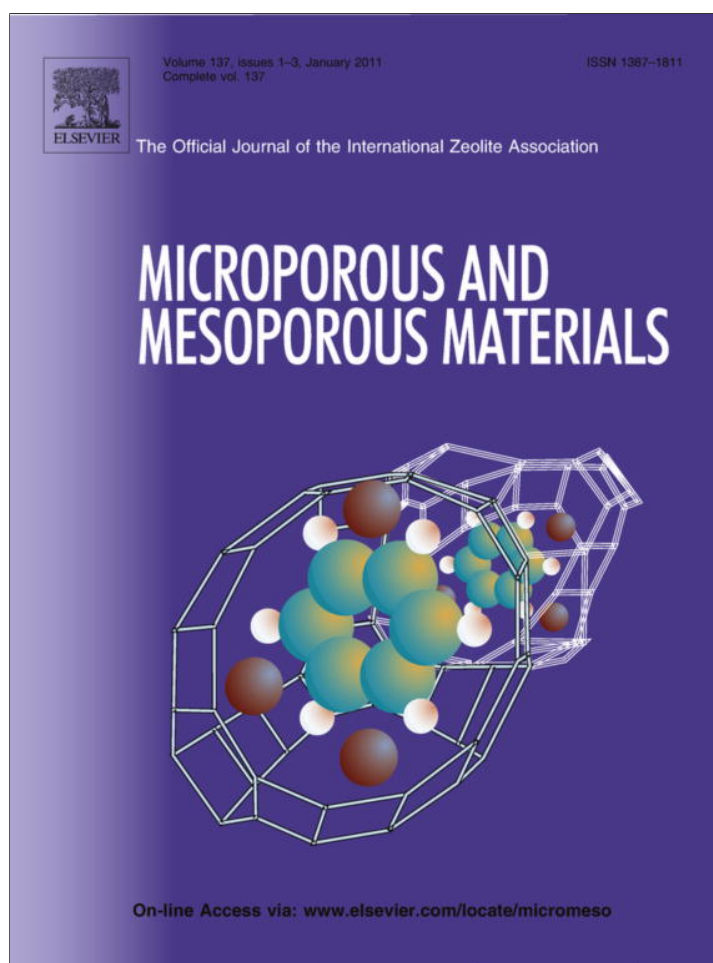


Provided for non-commercial research and education use.
Not for reproduction, distribution or commercial use.



(This is a sample cover image for this issue. The actual cover is not yet available at this time.)

This article appeared in a journal published by Elsevier. The attached copy is furnished to the author for internal non-commercial research and education use, including for instruction at the authors institution and sharing with colleagues.

Other uses, including reproduction and distribution, or selling or licensing copies, or posting to personal, institutional or third party websites are prohibited.

In most cases authors are permitted to post their version of the article (e.g. in Word or Tex form) to their personal website or institutional repository. Authors requiring further information regarding Elsevier's archiving and manuscript policies are encouraged to visit:

<http://www.elsevier.com/copyright>



Contents lists available at SciVerse ScienceDirect

Microporous and Mesoporous Materials

journal homepage: www.elsevier.com/locate/micromeso

Combined on-line differential mobility and particle mass analysis for determination of size resolved particle density and microstructure evolution

Q. Liu^a, X. Ma^{a,b}, M. R. Zachariah^{a,b,*}^a University of Maryland, College Park, Maryland, USA^b National Institute of Standards and Technology, Gaithersburg, Maryland, USA

ARTICLE INFO

Article history:

Received 6 July 2011

Received in revised form 10 November 2011

Accepted 11 November 2011

Available online 5 January 2012

Keywords:

Mobility analysis

Porosity measurement

Density measurement

ABSTRACT

A new application of on-line tandem differential mobility-particle mass analysis (DMA-APM) is used to obtain the density distribution, detect the reaction evolution, and investigate the mechanism of porous particle formation. The expected uncertainty of the density measurement is within 5%. The method has several advantages over absorption methods such as BET in which pore model is required. The methodology also enables a size resolved measurement to understand how particle porosity varies over a given particle population. The DMA-APM method is materials independent, and can measure the density even in a particle with inaccessible pores. In this paper we demonstrate the method during the synthesis of mesoporous iron oxide and copper oxide. For example in the formation of iron oxide we found that small particles (~50 nm) in the size distribution had a higher density (~2.6 g/cm³) relative to larger 130 nm particles with a measured density of 2.2 g/cm³. Syntheses at higher temperatures lead to high density particles which were also less size sensitive.

© 2011 Elsevier Inc. All rights reserved.

1. Introduction

Nanoparticles are being explored for a wide range of applications including their use in medicine, electronics, biomaterials and energy production. One important sub-class of nanomaterials is porous particles which can possess very high surface/volume ratio, and have application to drug delivery, absorbants or catalysts [1]. For example, iron oxide is being considered as a vehicle for drug delivery because its magnetic properties enable heating, directed motion, as well as *in vivo* monitoring [2].

Fig. 1 and Table 1 give important definitions and characteristics of different types of porous materials. Characterization of porous solids and powders includes surface area, pore size and density measurement. Usually, pore size and surface area can be characterized by Mercury Porosimetry or by gas adsorption methods such as Brunauer–Emmett–Teller (BET) approach. Mercury Porosimetry can typically be applied over the range 3.5 nm–500 μm. However, this method requires that the material be inert to mercury, and care must be taken to prevent creation of artificial pores due to powder packing. This leads to difficulties in the characterization of fine spray-dried powders and small-pore containing samples.

The most common gas for adsorption measurements, is nitrogen. However, the molecule is sufficient large so as to prevent

penetration into the smallest pores of interest, and has been shown to be inaccurate for measurement of low-surface-area material [3]. Some other alternative gases like water and dipole molecules, can enter very small pores, but the possibility of chemisorption makes the analysis more complicated [4]. Because the BET method requires an absorption model, the resulting extracted surface area and pore volume is highly dependent on the microscopic model employed and its validity for the specific system. As such the method itself suffers from absolute accuracy but is comparatively sensitive to changes within a given material system. The hysteresis loop of adsorption isotherms is also used to determine the pore size, and as an indicator of pore connectivity. However, the isotherms are complex to analyze due to the mixture of pore types and a wide pore size distribution typically found in porous materials.

Though we can estimate the porosity of a material by adsorption methods, the disagreement with the calculated specific surface area can be very large [5]. The uncertainty again comes from the model assumptions for the BET method: that the Kelvin equation is applicable over the complete mesopore range; the meniscus curvature is controlled by the pore size and shape; the pores are rigid and of well-defined shape; the filling or emptying of each pore does not depend on its location within the network; the adsorption on the pore walls proceeds in exactly the same way as on the corresponding open surface. Finally, the universal limitation of all adsorption methods is that the closed pores are not accessible to

* Corresponding author.

E-mail address: mrz@umd.edu (M. R. Zachariah).

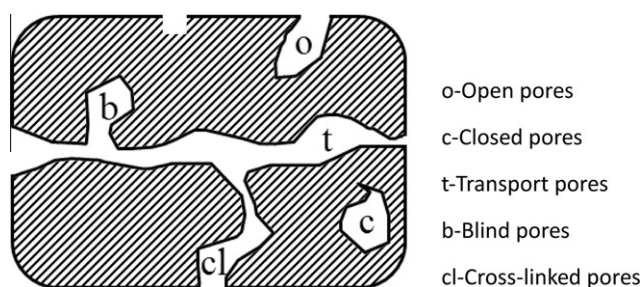


Fig. 1. Cross-section of porous material.

Table 1
Definitions of porous structures.

Open pore	Cavity or channel with access to the surface
Blind pore (dead-end pore)	Pore with a single connection to the surface
Closed pore	Cavity not connected to the surface
Total porosity	Ratio of volume of voids and pores (open and closed) to volume occupied by solid
Open porosity	Ratio of volume of voids and open pores to volume occupied by solid

the absorbants. Therefore, the porosity induced from these methods is the open porosity, not the total porosity.

Another important property is density, which requires measurements of mass and volume. However, it is difficult to measure the volume directly from the geometry of the object if the sample has an irregular shape; or by fluid displacement if the sample is a fine powder. There are some density measurement methods for liquid sample, including pycnometry and hydrometry [6]. However, the measurement of density in nanoparticles is still a topic of research.

In this paper, we develop a model and material-free method to measure the particle density by direct measurement of the mass and volume of particles. The measurement employs two different electrostatic manipulations of particles in series, which separately measures the size and mass. For porous particles of the type explored in this paper it also allows us to determine porosity of the sample with a much higher accuracy than that from BET methods and can do so independent of whether the pores are externally accessible or not.

2. Measurement methodology

The two methods to be employed in series to determine porosity and pore volume both employ charged particles that are manipulated within a static electric field with either drag (DMA), or centrifugal (APM) as the balancing opposing force.

2.1. Differential mobility analysis (DMA)

The DMA operates by selecting particles based on a balance of electrical and drag forces [7]. Particles exit the DMA based on a balance of electrical (F_E) drag forces (F_D).

$$F_D = F_E \Rightarrow \frac{3\pi\mu d_p}{C_c} v = neE \quad (1)$$

where n is the number of charges ($n = 1$ in our analysis), e is the unit of charge, E is electrical field strength, μ is the gas viscosity, C_c is the velocity slip correction factor, needed for particle in the free molecule flow, and v is particle velocity.

Eq. (1) shows a unique relationship exists between the particle mobility diameter, the measured velocity, and the applied electric field. At fixed electrostatic field only one mobility size will exit the instrument which can either be counted or sent to another instrument for further characterization. More detailed discussion on DMA operation was previously reported by Kim et al. [8].

Because we are employing ion-mobility methods, particles are first charged to a Boltzmann charge distribution by exposing the nanoparticle aerosol to a Po-210 radiation source. This enables a known charge distribution on particles, and for fine particles such as those in this study we work with singly charged particles [8].

2.2. Aerosol particle mass analyzer (APM)

The second instrument employed is an Aerosol particle mass analyzer (APM) [9]. The APM operates by balancing electrostatic and centrifugal forces, such that at a fixed applied electric field and rotation speed particles of only one mass will pass through the instrument.

$$m\omega^2 r_a = \frac{qV}{r_a \ln(r_2/r_1)} \Rightarrow \frac{m}{q} = \frac{V}{\ln(r_2/r_1) r_a^2 \omega^2} \quad (2)$$

where m is the particle mass, ω is the APM angular speed, V is the applied voltage, q is the particle charge, r_1 , r_2 and r_a are inner, outer and rotating radii at the equilibrium, respectively.

This instrument provides a direct relationship between applied voltage, rotation speed and the particle mass, and effectively operates as a mass spectrometer.

2.3. Combining the DMA and APM

As discussed above, the DMA directly measured mobility diameter, which for a sphere yields particle volume. The APM directly measures mass. The combination of volume and mass, provides a density.

In prior work we have measured the density of solid particles [10] to understand the mechanism of kinetics and mechanisms of metal nanoparticle oxidation [10–12]. Recently, this method has also been extended to density measurement of non-solid particles, such as carbon nanotubes [13] and silica aggregated particles [14].

In prior work we have estimated the uncertainties of the combined DMA-APM system. The theoretical uncertainty is estimated to be 5%, which is based on the transfer functions of the DMA, and APM [10–12]. Our prior experimental work on density measurements of reference particles yields an uncertainty of 4% [13] and mass measurements on NIST SRM 60 and 100 nm PSL spheres using combined DMA-APM were within about 1.4% and 5.6%, respectively [15].

In this paper we will implement a combined DMA-APM approach to measure the density of porous particles, compare with BET results, and use the results to conjecture a mechanism of formation. While the particles being characterized in a recreated aerosol phase the methodology can be implemented on particles dispersed in liquid phase by electrospray generation [16]. One significant advantage of this method is that the measurement method does not depend on the composition of the material but only on its physical parameters (volume and mass).

3. Experimental approach

The experiment system consists of two parts: (1) material preparation, (2) size and mass measurement. In addition, transmission electron microscopy (TEM, JEM 2100 FEG), X-ray diffraction (XRD, Powder Diffractometers for Materials Characterization) and

Brunauer–Emmett–Teller (BET, TriStar II 3020) analysis are used to confirm some of our findings and contrast results.

3.1. Preparations of porous Fe₂O₃ nanoparticles

To demonstrate the method we need a reliable source of porous material, which we adapt from prior work we have conducted on synthesis of porous particles by spray–pyrolysis methods to create porous iron oxide. A 0.2 M aqueous solution of iron (III) nitrate nonahydrate is sprayed using a collision-type nebulizer. The initial mean droplet size is about 1 μm in diameter as in our previous work [17]. The droplets are dried by passing them through a silica gel diffusion dryer. The aerosol is then passed through a tube furnace with temperatures set from 100 to 600 °C to decompose the precursor and create the porous iron oxide. Particles exiting the aerosol reactor are then collected on a 0.4 μm DTFP Millipore filter for the XRD and TEM characterization, or are directly sampled by the tandem DMA-APM system for analysis.

3.2. Preparation of hollow copper complex nanoparticles

A 0.2 M aqueous solution of copper (II) nitrate is sprayed with the nebulizer, and the aerosol droplets pass through a diffusion drier and a 600 °C furnace. Particles are collected on the filter for the XRD and TEM characterization, or are directly sampled by the tandem DMA-APM system for analysis.

3.3. Tandem DMA-APM

Fig. 2 shows the configuration used in this study, where the first three steps are to generate the particles, followed by DMA-APM density measurement. Essentially, we use the DMA to size select particles, which for a spherical particle defines its external volume. The size selected particles are then passed to the APM which selects particles by mass. Particles are then counted by a condensation particle counter. The combination of particle volume and mass defines density, and if we know the theoretic density of the material we can extract porosity.

3.4. Density and porosity determination

At a fixed DMA voltage (fixed particle size), an APM mass distribution from scanning APM voltage (rotation speed was kept constant at 3000 rpm) was fit to a Gaussian distribution to give a peak mass for a DMA selected particle size. Using this approach the densities ρ of various size particles generated under different conditions can be determined.

$$\rho = \frac{m}{V} = \frac{6m}{\pi d_p^3} \quad (3)$$

where d_p is the particle diameter from the DMA; m is the measured APM mass for that size particle.

The density measurement is independent of the material type, however a porosity (ϕ) determination requires referencing to the theoretical solid density (ρ_s).

$$\phi = \frac{V_p}{V} = \frac{\frac{m}{\rho} - \frac{m}{\rho_s}}{\frac{m}{\rho}} = 1 - \frac{\rho}{\rho_s} \quad (4)$$

The porosity measured is of all the pore space in the particle independent of whether the pores are accessible or closed and thus is different from the measurement from BET.

4. Result and discussion

4.1. Density measurement of porous iron oxide particles

4.1.1. Effective density and comparison with BET measurement of iron oxide

Representative XRD analysis of the produced particles is shown in the supplemental data (Fig. S1) demonstrates that Fe(NO₃)₃ has been converted to γ -Fe₂O₃. The broadened peak in the XRD patterns is attributed to small crystalline grain sizes (~10 nm or less) and microstrain from the fast growth of particles, including non-uniform lattice distortions, faulting, dislocations, antiphase domain boundaries and grain surface relaxation [18]. Because the decomposition of the nitrate to Fe₂O₃ occurs around 150 °C [19], we can assume that particles generated at 400, 500 and 600 °C are iron oxide.

Fig. 3 shows TEM images of the prepared particles as a function of furnace temperature. TEM images show that the particles are overall highly spherical with a porous internal structure. The porous structures of the particles are very sensitive to the synthesis temperature: higher temperatures lead to larger pores.

The solid density of γ -Fe₂O₃ is 4.9 g/cm³, which we will use to calculate the porosity. Because samples made at low furnace temperatures may not be phase pure γ -Fe₂O₃, and possibly more hydrated, we cannot obtain precise porosity for these samples, although the density measurements are still valid.

The DMA-APM results are summarized in Table 2 and show that the density increases monotonically from about 2 g/cm³ at 100 °C to about 3.4 g/cm³ at 600 °C. However the resulting porosity measurements for the 400–600 °C measurements show that even though the pore size increases as the furnace temperature increases, the porosity decreases.

Porosity can be induced directly from the density of porous particles, or combining with the BET data – pore volume per unit mass, the BET porosity can be described as:

$$\phi' = \frac{V_p}{V} = \frac{V'_p \times m}{m/\rho} = V'_p \times \rho \quad (5)$$

Table 3 shows the BET results and calculated porosity according to the BET data. The porosity calculated from BET is an order of magnitude lower than that determined from DMA-APM density data. Furthermore, a cursory inspection of the TEM images of Fig. 3(c), would suggest that the void volume must be considerably larger than the 6% value determined from BET. In addition, the BET determined external surface area (surface area excluding micro-pore surface) is larger than the BET total surface area in Table 3, so the difference between these two surface areas which is the

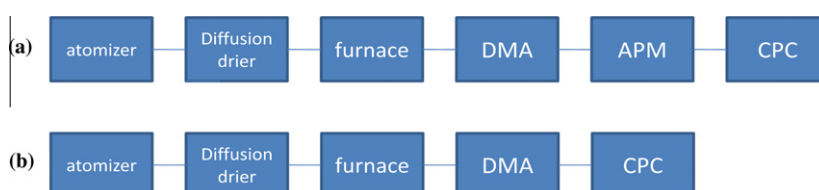


Fig. 2. Experiment methodology (a) online density measurement; (b) size distribution measurement after furnace.

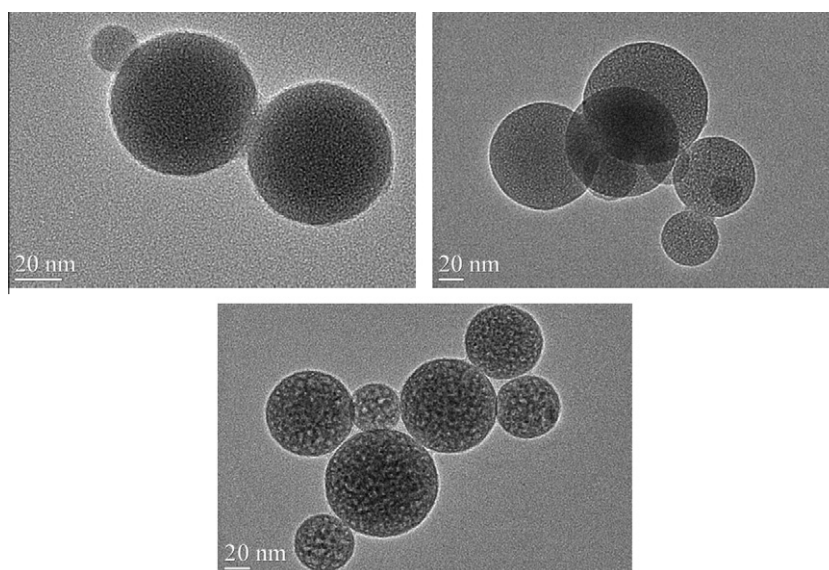


Fig. 3. TEM images of iron oxide particles generated at (a) 400 °C, (b) 500 °C, and (c) 600 °C.

Table 2

Results from tandem DMA-APM method.

Sample no.	1	2	3	4	5	6
Furnace temperature (°C)	100	200	300	400	500	600
Average density (g/cm ³)	2.09	2.11	2.46	3.12	3.22	3.44
Porosity	–	–	–	0.36	0.34	0.30
Peak size (nm)	88.2	94.7	82.0	71.0	66.1	63.8

Experiment not conducted. Because particles are not well crystallized to γ -Fe₂O₃ at low temperature, porosity which depends on the density of crystalline material cannot be accurately determined.

surface area of the micropores is negative, and this obviously is erroneous. This occurs because two different models are employed, which illustrates an inherent incompatibility in the BET result, due to this method's strong model dependence.

BET methods are nominally the standard method to compute open porosity. Though the pore volume and surface area are clearly incompatible and likely both are inaccurate, possibly due to poor connectivity in pore structure, the trend observed in pore diameter seems to be consistent with the TEM images in Fig. 3, probably from the accessible pore information.

On the other hand, given the demonstrated accuracy of the DMA-APM method as discussed previously, we should expect that the density measurement is highly reliable, and thus by inference the porosity should be more reliable than that determined from BET. However, because the DMA-APM method does not rely on any physics of the internal structure we cannot use this method to determine pore characteristics, and a reliance on BET is necessary.

4.1.2. Density distribution within a particle population for iron oxide

One of the significant advantages of the DMA-APM method is that it does not require macroscopic quantities to make a measure-

Table 3

BET characterization results.

Sample no.	4	5	6
External surface area (m ² /g)	14.2	9.3	6.6
Total surface area (m ² /g)	11.5	7.26	5.0
Single point absorption of pores (V'_p -cm ³ /g)	0.02	0.015	0.018
Porosity	0.062	0.049	0.062
Absorption average pore diameter (Å)	69.1	84.3	142.6

ment. Furthermore, the inherent size fractionation of the material is integral to the measurement and thus amenable to density and porosity measurements as a function of particle size, which cannot be done by other methods. This is important because in any typical bulk synthesis process, one expects to produce a range of particle size that represents the overall size distribution. In the context of creating porous structures one might also expect that there is a range of porosities that might be created that depend on particle size.

Fig. 4 shows density measured as a function of DMA selected particle size. The results show that at the highest temperatures of synthesis (600 °C) the density is independent of particle size. However, at lower temperatures, the density starts out at a lower level and decreases monotonically as particle size increases. This suggests that the synthesis was not complete at lower temperatures. If temperature or time were not sufficient, the largest particles would show the biggest effects. This is in fact clearly seen in Fig. 5, where the full range of particle population is imaged. The largest particle at the lowest temperature has the lowest density, and shows a monotonic increase in density approaching the higher temperature cases as particle size is decreased. These results indicate that the DMA-APM method has the potential to understand the kinetics of the pore formation process.

4.1.3. Pore structure creation

The results in Table 2 shows that average particle density increases with reaction temperature, but that the overall particle size decreased. There are two likely factors which could cause such a trend in density: gas generation during synthesis and sintering. Since the decomposition temperature of the nitrate is low (~125 °C), we expect that gas generation occurs first to make a porous structure. Higher temperatures should lower the viscosity of the melt allowing for the gas to escape easier, and thus creating a more dense structure before being frozen in. A lower viscosity melt will also induce more channeling effects which will tend to merge gas zone and thus produce larger pores as observed in the TEM images [20]. While this occurring grain growth is likely to increase the primary particle size and collapse of pores, which will lead to higher average pore size and a lower total pore volume.

Up to 200 °C the peak particle size increases, consistent with gas generation puffing the particle out like a balloon. Starting below 200 °C, gas generation dominates the size trend according

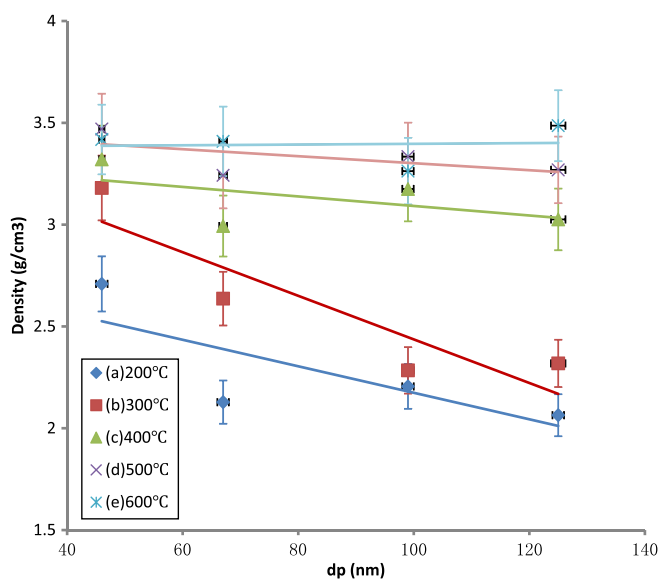


Fig. 4. Iron oxide particle density as a function of particle diameter, for different process temperature conditions. The error bars represent the 5% uncertainty for density and 1% uncertainty for particle diameter. Mass of the particles of a particular size is determined from the peak of the log normal distribution of number concentration vs. mass.

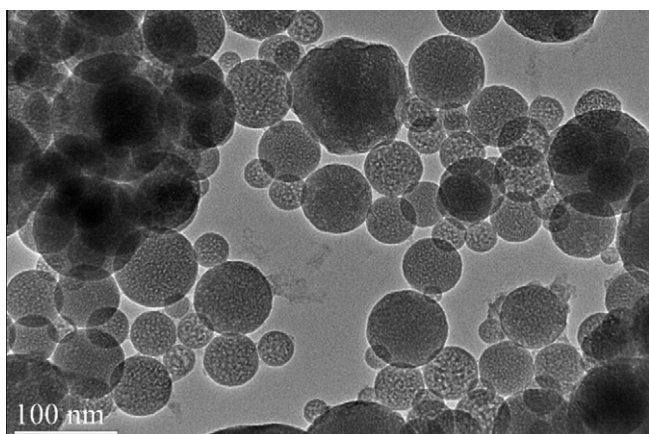


Fig. 5. TEM image of iron oxide showing the range of particle porosity and size in sample 5.

to the amount of gas emitted. Above 200 °C there is a steady decrease in the size distribution with increasing temperature. In this case all the gas generation whose tendency is to increase particle size is apparently offset by the tendency to collapse the structure.

4.1.4. Identifying the particle precursor

While our starting precursor is $\text{Fe}(\text{NO}_3)_3$ there is no particular reason to expect that after aerosolization and drying, the remnant precursor particle (before it enters the furnace) is still a nitrate. One possibility is that $\text{Fe}(\text{NO}_3)_3$ droplets hydrolyze to form solid phase $\text{Fe}(\text{OH})_3$ particles before reaction furnace, which then dehydrates in the furnace to make porous Fe_2O_3 (hydrolyzation occurs first). The second possibility is that, $\text{Fe}(\text{NO}_3)_3$ aqueous droplets form pure nitrate particle which decompose to Fe_2O_3 and oxynitride to make pores (nitrate decomposes directly).

In Table 4 we list the solid densities of iron hydroxide, iron nitrate and iron oxide. If we compare the densities of iron nitrate and

Table 4

Density of various iron containing compounds.

Pure composition	Iron hydroxide	$\text{Fe}(\text{NO}_3)_3 \cdot 9\text{H}_2\text{O}$	$\gamma\text{-Fe}_2\text{O}_3$
Density (g/cm^3)	3.4–3.9	1.68	4.9

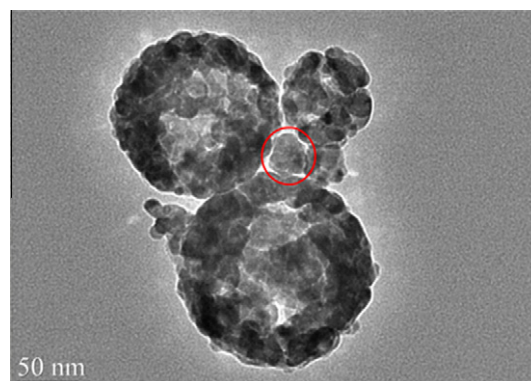


Fig. 6. TEM analysis of hollow copper complex particles. The red circle shows that some of the smaller particles may not be hollow. (For interpretation of the references in colour in this figure legend, the reader is referred to the web version of this article.)

the hydroxide with the measured densities of the particle at lower heating temperatures (Table 2) at the lowest temperature (100 °C), which is below the thermal decomposition temperature of nitrate, we measure a density above that of pure nitrate, indicating that the precursor particle is not the nitrate, or at least a mixture of the nitrate and the hydroxide precursor. Below 100 °C, solvent water is not fully evaporated yet, which implies that an intermediate of solid $\text{Fe}(\text{NO}_3)_3$ cannot exist in this fast evaporation process and would seem to confirm the first hypothesis that $\text{Fe}(\text{OH})_3$ forms before the solvent fully evaporates.

4.2. Density measurement of hollow copper oxide particles

In this second example we generate hollow CuO particles by spray pyrolysis. XRD analysis of the second sample is shown in the supplemental data Fig. S2, and demonstrate that $\text{Cu}(\text{NO}_3)_2$ has only partially been converted to CuO when heated at 600 °C for a residence time of 1 s. Compared to iron oxide, the primary particle (grain) size is significantly larger, which is confirmed in the TEM image of Fig. 6. More importantly the image clearly shows that particles have a hollow structure, which is very different from the porous iron oxide particle. Analysis of the XRD pattern indicates that copper oxide constitutes about 75% of the crystalline particle. The density of $\text{Cu}_2(\text{OH})_3(\text{NO}_3)$ and CuO is 3.4 and 6.3 g/cm^3 , respectively, so the mass average solid density used to calculate particle's porosity is 5.6 g/cm^3 . Compared to our measured particle density of $\sim 1.2 \text{ g}/\text{cm}^3$, the calculated porosity is 0.79.

As we discussed previously, the BET method is best employed for a regular pore structured material. Thus a hollow particle is not amenable to a BET type measurement, and illustrates some advantages in the uses of the DMA-APM approach.

Table 5

Measured density of copper oxide as a function of particle size.

Diameter (nm)	46	67	84	99	112	125	137
Density (g/cm^3)	1.6	1.2	1.2	1.2	1.1	1.1	1.2

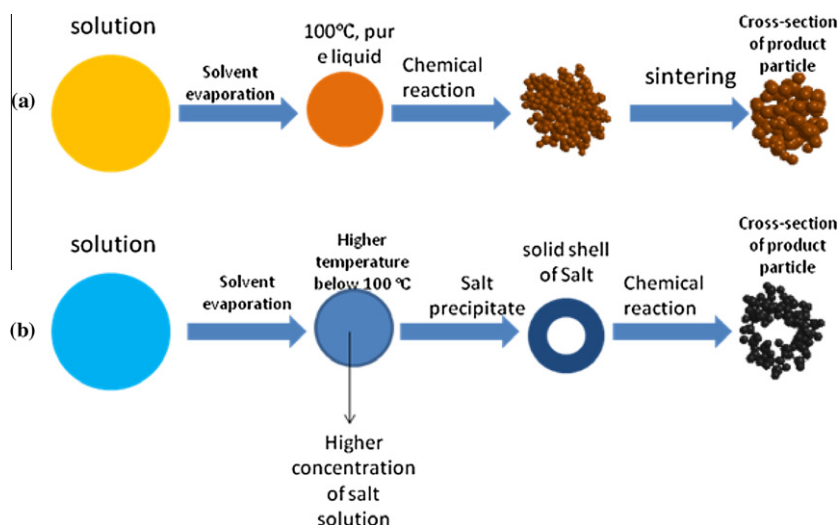


Fig. 7. Particle formation mechanism from precursors of (a) iron nitrate and (b) copper nitrate.

Table 6

Melting point and decompose temperature of nitrates.

Stable state precursor	Fe(NO ₃) ₃ ·9H ₂ O	Cu(NO ₃) ₂ ·3H ₂ O
Melting point (°C)	47	114
Decompose temperature (°C)	100–150	170

4.3. Particle formation models and verification

Table 5 shows that the density of copper complex particle is constant at 1.1–1.2 g/cm³, across all particle sizes, unlike the iron oxide case. The highest density (1.6 g/cm³) for the smallest particle sizes probably results from the fact that some of the smaller population sizes as seen from TEM are probably not hollow (see circle in Fig. 6).

The formation of hollow particles in spray pyrolysis is well known [21]. The prevailing wisdom is that solvent evaporation from the droplet occurs faster than the internal solute diffusion, thus the concentration of the solute near the outer edge of the droplet reaches its solubility limit and precipitates to form a shell. This shell is then converted to the metal oxide in the pyrolysis step.

In Fig. 7 we show a conceptual model for the formation of particles from spray pyrolysis for the two classes of materials observed. Table 6 shows that the melting point of iron nitrate is lower than the boiling point of the solvent water, so even if the concentration of salt exceeds the solubility on the shell in the evaporation process, the entity is still a fluid before chemical reaction, and thus always behaves like a droplet; i.e. there should be no shell structure formation before chemical reaction and the porous structure is primarily driven by gas generation and sintering.

However, for the copper nitrate, the melting point is higher than the boiling point of water, so precipitation can occur before the solvent is fully evaporated. Evaporation of water from the droplet results in local increases in solute concentration near the droplet edge leading to precipitation locally, and the formation of a crust. Subsequent decomposition/reaction freezes-in this hollow structure.

5. Conclusion

In summary, we demonstrate an on-line method to measure size resolved density of porous particles. The method relies on combining a differential mobility analyzer (DMA) with a particle

mass analyzer (APM) to make a simultaneous size resolved measurement of size and mass, from which density and porosity can be determined. We determined the expected uncertainty of the density measurement to be within 5%.

The method has several advantages over absorption methods such as BET in that no pore model is required, is materials independent and will measure the density even in a particle with inaccessible pores.

As shown in this work the method can be used to monitor pore evolution and deduce likely mechanism of microstructure formation.

Acknowledgments

Support for this work comes from a NSF-NIRT Grant. In addition, the authors wish to acknowledge the microscopy support through the University of Maryland Nanocenter, Dr. John T. Fourkas for the BET characterization support and Peter Y. Zavalij for the X-ray diffraction assistance.

Appendix A. Supplementary data

Supplementary data associated with this article can be found, in the online version, at doi:10.1016/j.micromeso.2011.11.017.

References

- [1] D. Vollath, *Nanomaterials: An Introduction to Synthesis Properties and Application*, Wiley-VCH, 2008.
- [2] W. Schartl, *Nanoscale* 2 (2010) 829–843.
- [3] H. deJonge, M.C. Mittelmeijer Hazeleger, *Environ. Sci. Technol.* 30 (1996) 408–413.
- [4] U.S.R.M. Cornell, *The Iron Oxides: Structure, Properties, Reactions, Occurrences, and Uses*, Wiley-VCH, 2003.
- [5] A. Galarnau, D. Desplandier, R. Dutartre, F. Di Renzo, *Microporous Mesoporous Mater.* 27 (1999) 297–308.
- [6] Eren, H. 1999. Density Measurement. *Wiley Encyclopedia of Electrical and Electronics Engineering*.
- [7] W.C. Hinds, *Aerosol Technology: Properties, Behavior, and Measurement of Airborne Particles*, Wiley, 1999.
- [8] S.H. Kim, K.S. Woo, B.Y.H. Liu, M.R. Zachariah, *J. Colloid Interf. Sci.* 282 (2005) 46–57.
- [9] K. Ehara, C. Hagwood, K.J. Coakley, *J. Aerosol Sci.* 27 (1996) 217–234.
- [10] X. Ma, M.R. Zachariah, *Int. J. Hydrogen Energy* 35 (2010) 2268.
- [11] X.F. Ma, M.R. Zachariah, *J. Phys. Chem. C* 113 (2009) 14644–14650.
- [12] L. Zhou, A. Rai, N. Piekielek, X.F. Ma, M.R. Zachariah, *J. Phys. Chem. C* 112 (2008) 16209–16218.
- [13] S.H. Kim, G.W. Mulholland, M.R. Zachariah, *Carbon* 47 (2009) 1297–1302.

- [14] K. Park, D.B. Kittelson, M.R. Zachariah, P.H. McMurry, *J. Nanopart. Res.* 6 (2004) 267–272.
- [15] A.A. Lall, X.F. Ma, S. Guha, G.W. Mulholland, M.R. Zachariah, *Aerosol Sci. Technol.* 42 (2009) 1075–1083.
- [16] D.H. Tsai, F.W. DelRio, A.M. Keene, K.M. Tyner, R.I. MacCuspie, T.J. Cho, M.R. Zachariah, V.A. Hackley, *Langmuir* 27 (2011) 2464–2477.
- [17] A. Prakash, A.V. McCormick, M.R. Zachariah, *Nano Lett.* 5 (2005) 1357–1360.
- [18] H.K.a.L. Alexander, *X-Ray Diffraction Procedures for Polycrystalline and Amorphous Materials*, 2nd ed., John Wiley & Sons, 1974.
- [19] A.M. Gadalla, H.F. Yu, *J. Mater. Res.* 5 (1990) 1233–1236.
- [20] L.Q. Ma, Z.L. Song, *Scripta Mater.* 39 (1998) 1523–1528.
- [21] H.F. Yu, W.H. Liao, *Int. J. Heat Mass Transfer* 41 (1998) 993–1001.